A&A 499, 905–916 (2009)
DOI: 10.1051/0004-6361/200810844

Astronomy & Astrophysics

Morphology and density structure of post-CME current sheets

B. Vršnak[1], G. Poletto[2], E. Vujić[3], A. Vourlidas[4], Y.-K. Ko[4], J. C. Raymond[5], A. Ciaravella[6], T. Žic[1], D. F. Webb[7], A. Bemporad[8], F. Landini[9], G. Schettino[9], C. Jacobs[10], and S. T. Suess[11]

[1] Hvar Observatory, Faculty of Geodesy, Zagreb, Croatia
e-mail: bvrsnak@geof.hr
[2] INAF-Arcetri Observatory, Firenze, Italy
[3] Faculty of Science, Geophysical Department, Croatia
[4] Naval Research Laboratory, Washington DC, USA
[5] Harvard-Smithsonian Center for Astrophysics, Cambridge, USA
[6] INAF-Palermo Observatory, Palermo, Italy
[7] Boston College and AFRL, Hanscom, USA
[8] INAF-Torino Astrophysical Observatory, Pino Torinese, Italy
[9] Dept. of Astronomy and Space Science, University of Florence, Italy
[10] Centrum voor Plasma-Astrofysica, K. U. Leuven, Belgium
[11] NASA Marshall Space Flight Center, Huntsville, USA

Received 22 August 2008 / Accepted 6 February 2009

ABSTRACT

Context. Eruption of a coronal mass ejection (CME) drags and "opens" the coronal magnetic field, presumably leading to the formation of a large-scale current sheet and field relaxation by magnetic reconnection.
Aims. We analyze the physical characteristics of ray-like coronal features formed in the aftermath of CMEs, to confirm whether interpreting this phenomenon in terms of a reconnecting current sheet is consistent with observations.
Methods. The study focuses on measurements of the ray width, density excess, and coronal velocity field as a function of the radial distance.
Results. The morphology of the rays implies that they are produced by Petschek-like reconnection in the large-scale current sheet formed in the wake of CME. The hypothesis is supported by the flow pattern, often showing outflows along the ray, and sometimes also inflows into the ray. The inferred inflow velocities range from 3 to 30 km s^{-1}, and are consistent with the narrow opening-angle of rays, which add up to a few degrees. The density of rays is an order of magnitude higher than in the ambient corona. The density-excess measurements are compared with the results of the analytical model in which the Petschek-like reconnection geometry is applied to the vertical current sheet, taking into account the decrease in the external coronal density and magnetic field with height.
Conclusions. The model results are consistent with the observations, revealing that the main cause of the density excess in rays is a transport of the dense plasma from lower to higher heights by the reconnection outflow.

Key words. Sun: coronal mass ejections (CMEs) – Sun: corona – Sun: solar wind – magnetohydrodynamics (MHD)

1. Introduction

According to our current understanding of solar coronal mass ejections (CMEs), the eruption of an unstable magnetic structure is closely associated with the formation of a large-scale current sheet (hereinafter CS) in the wake of the eruption. This concept was initially proposed and developed by Carmichael (1964), Sturrock (1966), Hirayama (1974), and Kopp & Pneuman (1976), connecting the large-scale eruption and the localized energy release in the form of flare (the so-called CSHKP model). When the current sheet becomes long enough, the tearing instability sets in, leading to fast reconnection of magnetic field (for the analytical, numerical, laboratory, and observational results, see, e.g., Furth et al. 1963; Ugai 1987; Gekelman & Pfister 1988; and Vršnak et al. 2003, respectively). Reconnection in the post-CME current sheet results in an abrupt energy release causing a flare, and also enhances and prolongs the acceleration of the erupting magnetic field structure (e.g., Lin 2004; Vršnak 2008, and references therein). Numerical MHD simulations covering various scales, from the low corona to 1 AU, also demonstrated post-CME current sheet formation, clearly revealing the importance of the reconnection in the initiation, acceleration, and propagation of CMEs (see, e.g., Riley et al. 2002; Roussev et al. 2003; Török et al. 2004; and Riley et al. 2007; and for a review, see Forbes et al. 2006).

The most prominent consequence of CME-associated reconnection is the appearance of the so-called two-ribbon flare, which is closely related to the CME acceleration stage (e.g., Maričić et al. 2007, and references therein). The ribbon expansion away from the magnetic inversion line, associated with a growing system of hot loops connecting the ribbons, has led to the formulation of the CSHKP model. The discovery of cusped structure above the flare loops (e.g., Tsuneta et al. 1992; Forbes & Acton 1996; Tsuneta 1996), loop-top hard X-ray sources (e.g., Masuda et al. 1994; Aschwanden et al. 1996; Sui et al. 2004; Veronig et al. 2006), the loop shrinkage (e.g., Švestka et al. 1987; Forbes & Acton 1996; Sheeley et al. 2004; Vršnak et al. 2006), and the recognition of growing post-eruption loop systems in the absence of flares, all provided further support of the CSHKP scenario. Additional evidence of reconnection below the erupting flux-rope may be found in the so-called disconnection events (e.g., Webb & Cliver 1995; Simnett et al. 1997; Wang et al. 1999), downflows above the post-eruption arcades (e.g., McKenzie & Hudson 1999; Innes et al. 2003a;

Asai et al. 2004), horizontal converging flows above the loops (Yokoyama et al. 2001; Lin et al. 2005), and flare-associated radio emission below the eruptive prominence (Vršnak et al. 2003).

Post-CME features detectable in UV spectra (Ciaravella et al. 2002; Ko et al. 2003; Innes et al. 2003b; Lin et al. 2005; Bemporad et al. 2006; Ciaravella & Raymond 2008), X-ray images (Sui et al. 2004, 2005), and white light coronagraph images (Ko et al. 2003; Webb et al. 2003; Lin et al. 2005) have been attributed to the current sheets expected to "connect" the flare loops to the CME core. The UV spectral signature is generally emission in the high temperature lines of Fe XVIII or Fe XIX formed at 5–10 MK. EUV images from the Extreme-ultraviolet Imaging Telescope (EIT) onboard the Solar and Heliospheric Observatory (SoHO) and the Transition Region and Coronal Explorer (TRACE) show emission in Fe XXIV at even higher temperatures (McKenzie & Hudson 1999; Innes et al. 2003a). The UV features decay slowly, on timescales of between several hours (Ciaravella & Raymond 2008) and a few days (Bemporad et al. 2006; Ko et al. 2003). The X-ray data from the Reuven Ramaty High Energy Solar Spectroscopic Imager (RHESSI) exhibit regions of high temperature emission above loop tops, and both the morphology at different energies and the evolution of the structures are consistent with the CS indentification. The white light features are bright, narrow rays that appear to connect the cusped flaring loop system to the CME core (Lin et al. 2005). Some show blobs of plasma moving outwards at several hundred km s^{-1}. Like the UV features, the white-light structures can last for a day or two. In general, white light observations reveal the electron column density, UV data constrain temperatures, emission measures, and Doppler shifts, and X-ray observations reveal very high temperature plasma.

The aim of this paper is to demonstrate that post-CME rays appear as a consequence of the reconnection in the current sheet formed in the wake of CME, and to quantify their basic physical characteristics. We outline the working hypothesis in Sect. 2, and provide details of the model used to compare the theoretical expectations with observations in the Appendix. We present in Sect. 3 our observations and measurements, focusing on the morphology and plasma densities in post-CME rays. The temperature structure and the ionization state will be presented in a separate paper. Our density measurements are compared with the model estimates and some previous empirical results in Sect. 4. Results are discussed and conclusions drawn in Sect. 5.

2. Working hypothesis

Since post-CME rays extend outward from cusped structures associated with growing post-eruption loop-systems, our working hypothesis is that they appear as a consequence of the reconnection in the CS formed in the wake of CME. Furthermore, we assume that the reconnection process can be described approximately in terms of the steady-state Petschek regime (Petschek 1964). In this regime, the reconnection takes place within a small diffusion region (DR), from which two pairs of standing slow-mode shocks (SMSs) extend along the axis of symmetry. Thus, the CS is bifurcated, SMSs separating the inflow and outflow region (Petschek 1964; Soward & Priest 1982). At SMSs, the inflowing plasma is compressed, heated, and accelerated, forming the upward and downward reconnection jet (Fig. 1). We note that electric currents are concentrated only in DR and SMSs.

When reconnection occurs in the homogeneous environment, the characteristics of outflowing plasma are determined primarily by the external plasma-to-magnetic pressure ratio,

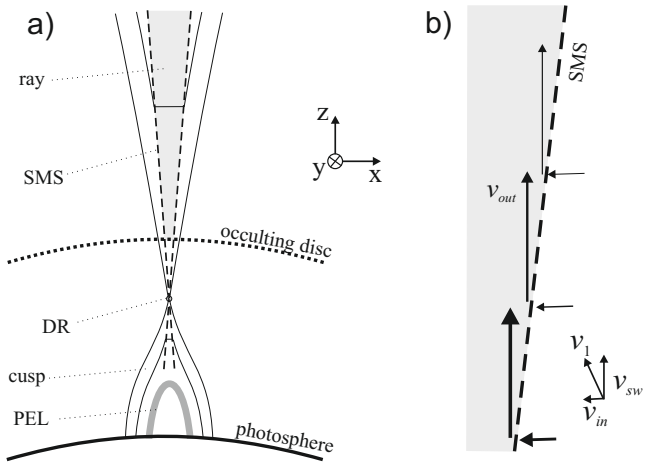

Fig. 1. a) Interpretation of the ray in terms of the Petschek (1964) reconnection model: DR – diffusion region; SMS – slow mode shocks (dashed lines intersecting at DR); PEL – post-eruption loops. Magnetic field-lines are drawn by thin lines; gray area between the SMSs outlines the post-CME ray. The coordinate system is indicated (the line of sight is in y-direction). **b)** An element of bifurcated current sheet; arrows mark plasma flows (v_{in} – inflow velocity; v_{sw} – solar wind speed; v_{out} – outflow speed), where the arrow thickness depicts plasma densities.

whereas the outflow speed is approximately equal to the external Alfvén speed (see Appendix in Aurass et al. 2002; and Skender et al. 2003). However, in the case of a vertical current sheet, the ambient coronal density and magnetic field decrease with height, so the characteristics of the reconnection jets also depend on height. The main effect is transport of the dense plasma from lower heights upward, which makes the outflow jet far denser than the ambient corona (see Appendix). In this respect, the post-CME ray should be similar to coronal streamers.

Bearing in mind the geometry of the Petschek-type reconnection, the post-CME CS should have distinctive morphological characteristics. It should be thinnest at the height of the diffusion region, and become wider with increasing height. In the homogeneous plasma, the angle between the SMSs is determined by the inflow Mach number (Soward & Priest 1982; Vršnak & Skender 2005), the half-angle typically equaling a several degrees (Vršnak & Skender 2005). Thus, for the CS length of several solar radii, the Petschek-CS thickness (the distance between the SMSs) is on the order of 100 Mm. We note that in the case of the vertical CS in the solar corona, where the magnetic field diverges radially, the angle between SMSs should increase with height even at uniform inflow Mach number (see Appendix), so the CS thickness should be somewhat larger than in the plane-symmetric case.

Further important characteristics of the post-CME CSs that determine their appearance in coronagraphic images, are the horizontal length and the orientation with respect to the line of sight (Fig. 2). We note that the angle θ between the plane of CS and the line of sight (LoS) must be rather small, otherwise the CS would not appear as a distinct feature in coronagraphic images. This causes a "selection effect", which can explain the fact that post-CME rays can be recognized only in a relatively small fraction of events (Webb et al. 2003).

In Fig. 2a, we depict how the effective thickness D of the ray depends on the CS thickness $2d$, horizontal length L, and the angle θ. On average, a ray should be thinner and brighter for smaller θ (larger LoS column-length λ). In Fig. 2b, we illustrate how the variation in θ along the LoS can account for the complex

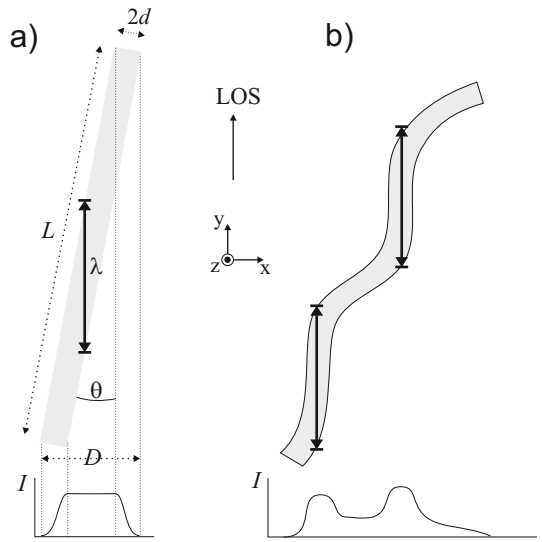

Fig. 2. Dependence of the width and morphology of the ray at a given height on the orientation/geometry of the current sheet: **a)** straight CS; **b)** wavy CS. The CS half-thickness is denoted by d, horizontal length (i.e., the length in xy-plane, see also Fig. 1) by L, the ray width by D, and the inclination to the line of sight (LoS) by θ. The plasma-column length λ is drawn by thick double-arrow. At the bottom the intensity profile is sketched.

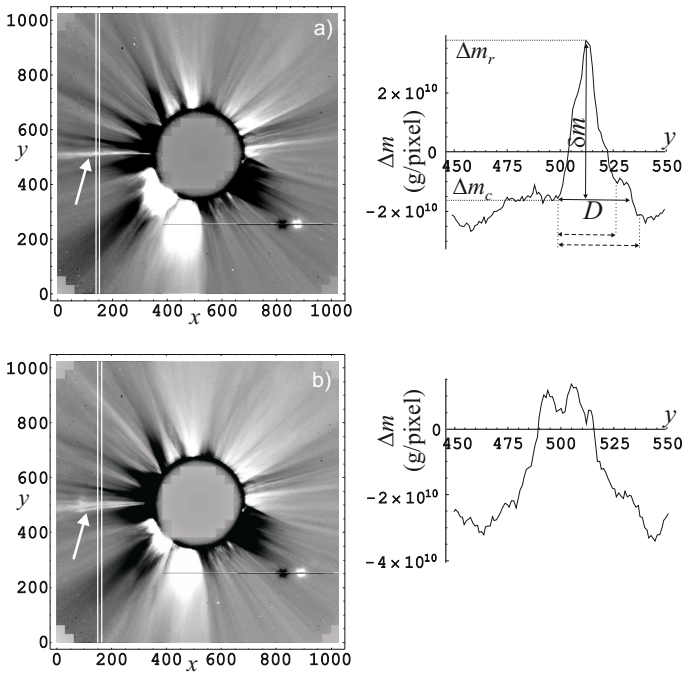

Fig. 3. a) Simple post-CME ray (9 January 2002 at 06:06 UT); **b)** complex ray consisting of three radial substructures (9 January 2002 at 02:30 UT). The ray is marked by white arrow. The scale of the LASCO-C2 images is given in pixels (1 pixel corresponds to 11.9 arcsec). The column-mass profiles measured along the bin marked by white lines are shown in the right-hand panels (abscissa scale in pixels). Estimates of the ray width, D, and column-mass excess, δm, are indicated in **a)**. Dashed arrows indicate the lower and upper limit of D.

appearance of the ray (see also Saez et al. 2007), i.e., a wavy CS would be seen by observer as a "multi-ray" structure. We note that the angle θ, or its variation along the LoS, can vary with both time and height, such that the morphology of the structure can change with time and can differ at different heights.

3. Observations

3.1. SoHO/LASCO mass images

To analyze the morphology and column density of post-CME rays, we employ data provided by the Large Angle Spectroscopic Coronagraph (LASCO, Brueckner et al. 1995) onboard SoHO. We focus on the LASCO-C2 images, which cover radial distances from 2 to 6 solar radii ($r_\odot$). We use, in particular, the so-called mass images derived from LASCO base-difference images calibrated in units of solar brightness. These images exhibit changes in the column mass along the line of sight under the assumption that the structure is in the plane of sky (for details we refer to Billings 1966; Poland et al. 1981; Vourlidas et al. 2000; and Vourlidas et al. 2002); bright pixels (positive values) represent areas where the column mass has increased, whereas dark pixels (negative values) show depleted regions.

We initially considered eleven post-CME ray events, which were spotted while analyzing the associated CMEs for other purposes, i.e., the rays were chosen rather randomly. Thus, no attempt was made to analyze the occurrence rate of post-CME rays (for the criteria and statistical background we refer the reader to Webb et al. 2003). Nevertheless, we note that ray-like features in the wake of CMEs are not uncommon, in particular when considering the specific circumstances under which a post-CME current sheet could be observed: i.e., the level of post-CME activity should not be too high, and the current sheet must be oriented at a small angle with respect to the line of sight and should be relatively stable.

Inspecting the selected sample, we noted intermittent activity in most of the rays, which manifests itself as changes in their shape, contrast, and inclination. These variations were either caused by coronal disturbances originating in remote eruptions, or were indicative of internal activity, such as blob formation/ejection and/or outward propagating wave-like perturbations.

For a detailed analysis, we chose three post-CME rays, observed on 8–9 January 2002, 18 November 2003, and 26 June 2005. The events of 18 November 2003 and 26 June 2005 were selected as examples of relatively stable rays. In both events, we analyzed only one ray image (at 12:50 UT and 06:30 UT, respectively). On the other hand, the event of 8–9 January 2002 did exhibit significant activity, similar to that in the remaining eight events. This event was selected to quantify the level of variability in post-CME rays, and we therefore performed measurements at three different times (00:06, 06:06, and 12:06 UT). We note that the rays in the selected exposures did not have significant blob-like features or similar inhomogeneities, although they might have been present at earlier and/or later times.

3.2. The ray morphology

In Fig. 3, we illustrate the variability in the ray morphology by showing two images of the ray that became recognizable a few hours after the east-limb CME eruption on 8 January 2002 (the first appearance in LASCO-C2 at 17:54 UT). In Fig. 3a, we first show a simple ray pattern that was recorded half a day after the eruption. Four hours earlier, the ray had a complex form consisting of three radial substructures (Fig. 3b); this "multi-ray" pattern could be caused by a wavy current sheet, as illustrated in Fig. 2b. Morphological changes of this kind, which develop on timescales of hours are a common characteristic of post-CME

rays, since they were present in nine of the eleven events in our initial sample.

Our estimates of the ray width and column-mass excess are based on the LASCO-C2 mass-images (Fig. 3 left), which for each pixel, provide the difference Δm between the column-mass in the actual image and the reference image. In the right-hand panels of Fig. 3, we show two mass-difference profiles $\Delta m(y)$, where Δm is expressed in g/pixel, while the abscissa, corresponding to the y coordinate of the LASCO images, is represented in pixels. The profiles shown were measured in the LASCO-C2 difference-images along the bin marked by white lines in the left panel of Fig. 3, i.e., roughly perpendicular to the ray direction. The bin is 10 pixels wide, and the profile shows Δm averaged over the bin width. Pixels with $\Delta m = 0$ represent areas where the column-mass remained the same as it was in the reference image. We note that the mass aside the rays is depleted ($\Delta m < 0$), probably due to the CME-associated coronal expansion, usually seen as coronal dimming when the eruption is launched from regions on the solar disc. The depletion might also be caused partly by the presumed inflow into the current sheet.

Given the working hypothesis, where the ray is assumed to be the reconnection outflow jet of a large-scale Petschek-like bifurcated current sheet, we are interested in the column-mass excess of the ray, δm, defined as the difference between the peak in the ray column-mass Δm_r and the column-mass in the adjacent corona Δm_c. In other words, δm determines the difference of column-mass associated with the current sheet and the inflow region ($\delta m = \Delta m_r - \Delta m_c$; see the right-hand panel of Fig. 3a). The ray width D is measured as the full width of the ray structure in the mass-difference profile (Fig. 3a right). The main source of error in estimating δm and D is the determination of the value Δm_c, since this value is frequently different on opposite sides of the ray (Fig. 3a right). Thus, we estimated the upper and lower limit (dashed arrows in Fig. 3a right), and these measurements provided us with the error bars plotted in Fig. 4.

The measurements illustrated in Fig. 3 were performed on five images of post-CME rays for the LASCO-C2 range of heights to estimate the radial dependence of the relevant ray parameters. The measured rays are marked in the mass-images shown in the left column of Fig. 4 (hereinafter denoted as rays a–e). In the second column of Fig. 4, the ray widths, expressed in units of the solar radius $r_\odot$, are presented as a function of the radial distance, $D(R)$, where $R = r/r_\odot$. The ray in Fig. 4a is characterized by a "multi-ray" structure, and we therefore measured only the central feature, which was the most prominent element of the structure.

Inspecting the graphs, one finds that in the distance range of $R = 2$–2.5 the widths vary between 0.1 and 0.4 $r_\odot$ (mean value 0.26). In the range $R = 5$–6, the widths increase to 0.4–0.9 $r_\odot$ (mean 0.7). The widths that we found at $R \sim 2$ are more than twice as large as those found by Webb et al. (2003), who analyzed the coronagraph data obtained by the Solar Maximum Mission (SMM): converting their values of the width expressed in degrees, into units of the solar radius at the corresponding heights, we find that the mean width reported by Webb et al. (2003, see Tables 2 and 3 therein) is 0.09 $r_\odot$ in this height range. The difference may be related to the lower sensitivity of SMM.

3.3. The ray density

In the third column of Fig. 4, we show the radial dependencies of column-mass excesses $\delta m(R)$, expressed in g/pixel. Inspecting the graphs $\delta m(R)$, we find that the slopes of the fitted power-law functions range from −2.1 to −3.2, the average value being -2.6 ± 0.5.

The column-mass excess δm was converted to the number-density excess δn by assuming that, due to the spherical geometry, the column length increases in proportion to the radial distance, $\lambda \propto R$. In particular, we used $\lambda_0 = 100$ Mm at $R = R_0 = 2.16$ (the lowest height of measurements). The outcome is presented in log-log graphs in the fourth column of Fig. 4, together with the power-law fits. We note that some other choice of λ_0 would shift vertically the $\delta n(R)$ dependence, without changing the slope in a log-log graph. The slope would change only if some other radial dependence $\lambda(R)$ existed, e.g., the angle θ was height-dependent.

Inspecting the graphs $\delta n(R)$ in Fig. 4, we find that the slopes of the fitted power-law functions range from −3.1 to −4.2, the average value being -3.6 ± 0.5. We pay special attention to the slope of the fit, since it does not depend on the presumed value of λ_0, so it can be compared directly with the model results (Sect. 4.1). In this respect it is important to note that in the case of the smallest slope in the sample, the ray width becomes approximately constant beyond $R \approx 3$, indicating a possible decrease in θ with the height, i.e., an increase in λ. This would imply that in this case the densities are overestimated at larger heights, since $\delta n \propto \delta m/\lambda$, i.e., the true slope of $\delta n(R)$ is probably steeper.

Since the evaluation of the density excess depends on the choice of the column length λ, in Fig. 5 we present an estimate of the number of electrons per unit length of the ray, which is a parameter independent of λ. If we approximate the mass-difference profiles across the ray by triangular profiles, the mass-excess per unit length of the profile amounts to $M = D\delta m/2$, from which we evaluate the electron-number excess per unit length of the ray, N_e.

Inspecting Fig. 5a, where $N_e(R)$ is presented separately for all five rays from Fig. 4, we find that $N_e(R)$ either decreases (rays [a], [b], and [d]) or stays roughly constant (rays [c] and [e]). When averaged, the data from Fig. 5b show a dependence similar to that obtained by Ciaravella & Raymond (2008), who found that after a decrease at low heights, the value of N_e becomes approximately constant. Comparing their Fig. 8 with our Fig. 5b, we find that the numbers and trends are similar. However, the radial distance at which $N_e(R)$ becomes constant, differs: according to results by Ciaravella & Raymond (2008), this occurs at $R \approx 2$, whereas in our case the transition occurs at $R \approx 4$. In Fig. 5b, we also present the power-law fit, showing that the overall trend could also be described by $N_e \propto R^{-1}$.

3.4. Coronal flows

Coronal regions beneath CMEs are generally characterized by highly dynamical intricate structures, revealing complex magnetoplasma flows and waves. Consequently, it is difficult to identify persistent systematic flow patterns, especially during periods of increased solar activity, when disturbances from other CMEs affect the coronal region of interest. This also holds for flow patterns associated with post-CME rays, whose morphologies are permanently changing and are strongly affected by disturbances from distant CMEs.

In certain situations, some characteristic flows could however be identified. Most frequently, outward-moving inhomogeneities along the ray are observed, usually having velocities of several hundred km s^{-1} (e.g., Ko et al. 2003; Lin et al. 2005). Such motions are often interpreted in terms of the reconnection outflow, which may or may not be characterized by the Alfvénic

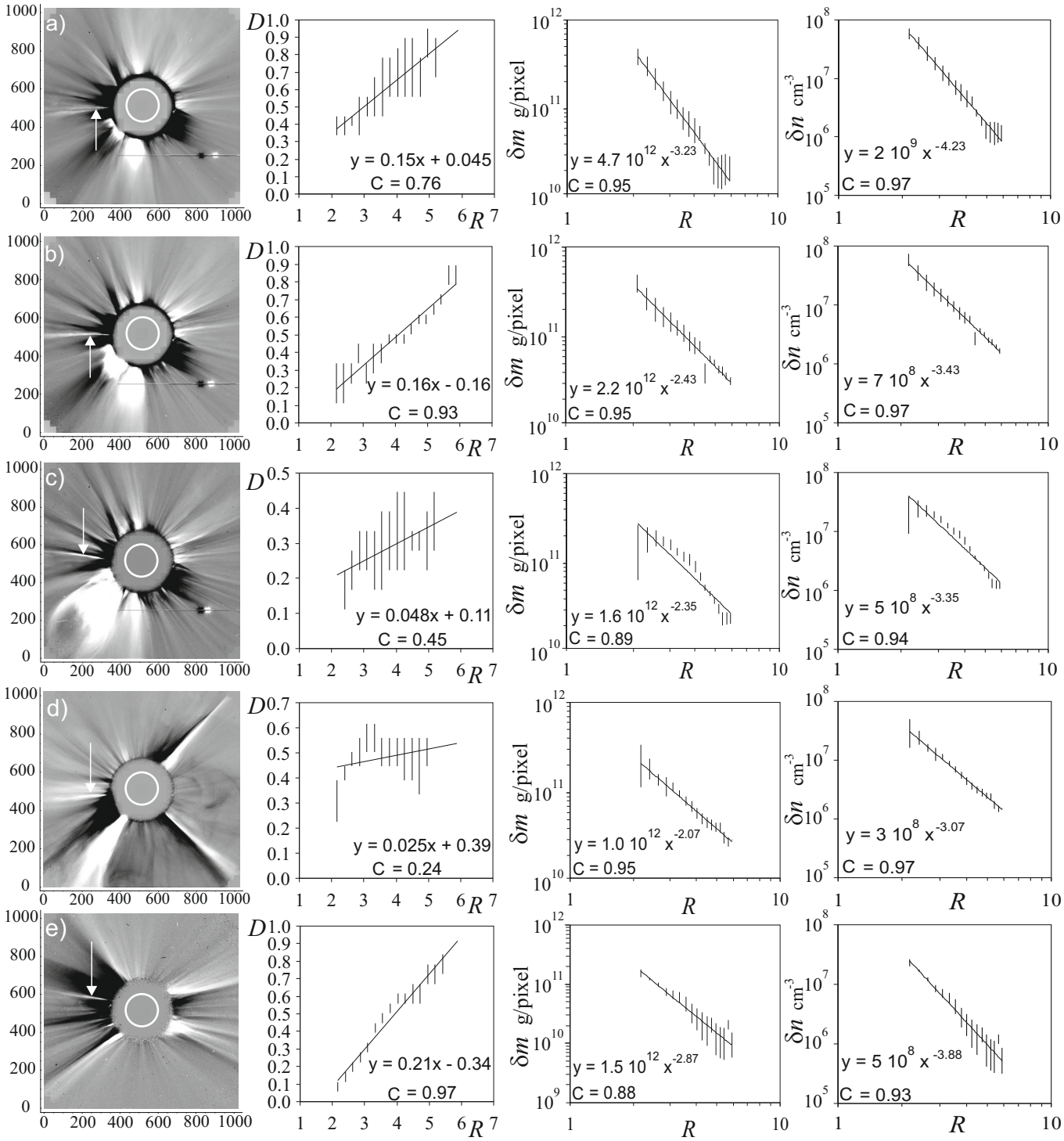

Fig. 4. The five measured post-CME rays (indicated by arrows in the full-resolution LASCO-C2 images shown in the first column): **a–c)** 9 January 2002 at 00:06, 06:06, and 12:06 UT, respectively; **d)** 18 November 2003 at 12:50 UT; **e)** 26 June 2005 at 06:30 UT. In the second, third, and fourth column we show the ray width, column-mass excess, and the density excess, as a function of the radial distance. The widths and radial distances are expressed in units of the solar radius. The least-square fits are shown in the insets, together with the correlation coefficient C.

speed (for a discussion we refer to Bárta et al. 2008, and references therein). In this respect, we note that signatures of shrinking loops are also observed occasionaly in the wake of CMEs (e.g., Sheeley & Wang 2002; Sheeley et al. 2004; Sheeley & Wang 2007, and references therein) consistent with decelerated reconnection downflows.

Compared to reconnection outflows, detecting signatures of reconnection inflows is far more difficult. A possible example was reported by Yokoyama et al. (2001), based on the observations by the EIT/SoHO. Another example was presented by Lin et al. (2005), who employed data from EIT and the UltraViolet Coronagraph Spectrometer (UVCS) onboard SoHO. Recently, Bemporad et al. (2008) reported a "side-reconnection" in the aftermath of a CME, induced by the CME expansion: from the detection of two converging reconnecting features at 1.7 $r_\odot$ (probably the CME flank and the streamer boundary), the authors

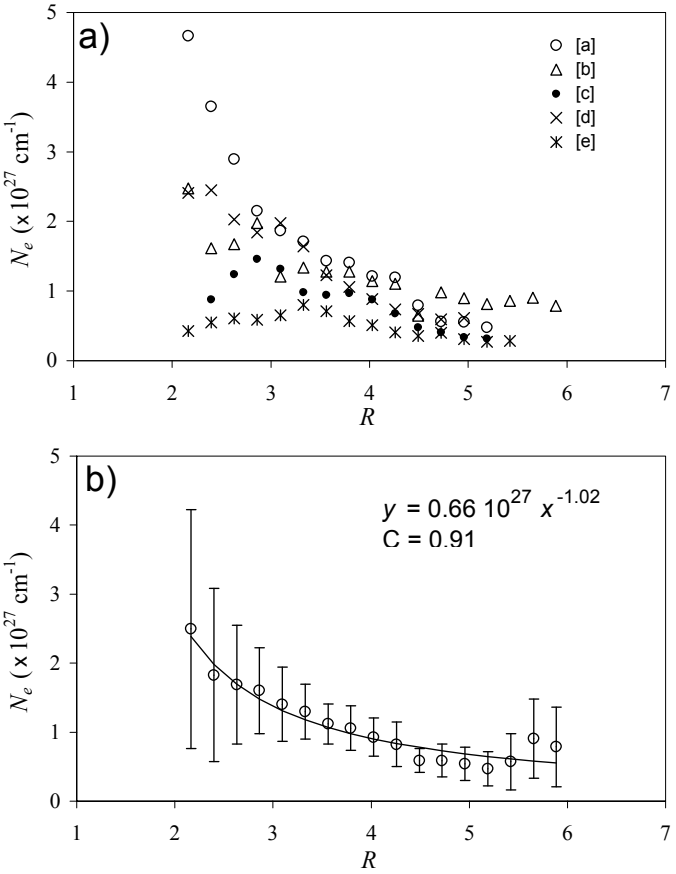

Fig. 5. Number of electrons per unit length of the ray, $N_e(R)$: **a)** presented separately for the five rays shown in Fig. 4 (measurements are labeled in the legend, following the sequence in Fig. 4); **b)** averaged over the five rays (error bars represent standard deviations), shown together with the power-law fit.

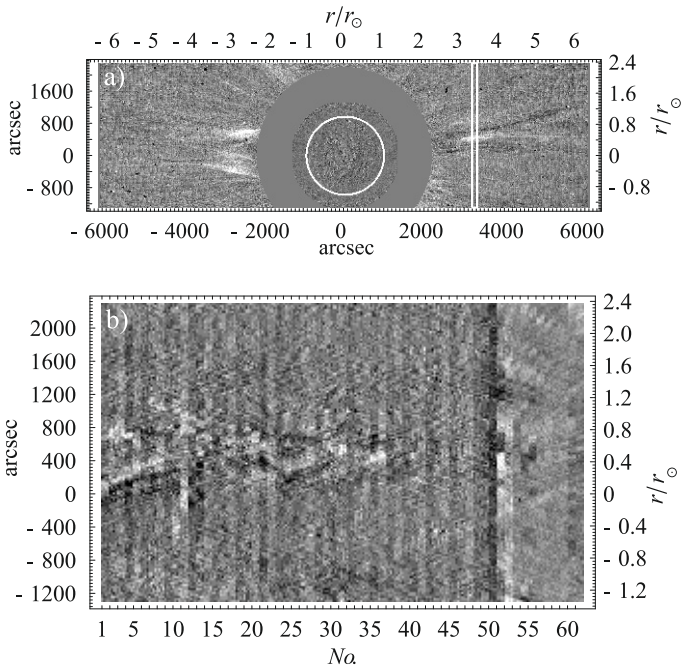

Fig. 6. **a)** LASCO-C2 running-difference images of the west-limb ray of 8 January 2002 (13:54 UT), revealing the inflow into the ray. The slice used in the stack-plot shown in **b)** is outlined by white rectangle centered at $x = +3.34\,r_\odot$. **b)** Stack-plot composed of slices taken from successive running-difference images; x-axis represents the ordinal number of the LASCO image for 8 January 2002.

inferred an inflow speed of 3–4 km s^{-1}, close to the 5 km s^{-1} derived by Yokoyama et al. (2001).

In Fig. 6, we present a stack-plot showing an example of the reconnection-inflow pattern observed above the west limb on 8 January 2002 in the LASCO-C2 field-of-view. We note that this post-CME feature is not the ray of 8–9 January 2002 presented in Figs. 3 and 4, which was on the opposite side of the solar disc. This west-limb event was not observed by UVCS, i.e., we do not know if it exhibited Fe XVIII emission, which is one of the criteria for identifying post-CME current sheets. We note that we could not detect a distinctive signature of reconnection inflow in the three post-CME rays analyzed in Sects. 3.2. and 3.3. In these events, no suitable inhomogeneities could be identified to provide tracing of plasma motion in the inflow region (to be discussed in Sect. 5).

The west-limb ray presented in Fig. 6, formed after a faint ejection that was first observed in LASCO-C2 at 02:54 UT on 8 January 2002 (not listed in the LASCO CME catalog). Each stack represents the cut along a line parallel to the y-axis of a given LASCO-C2 512×512-pixel running-difference image, showing the pixel-intensities in the range $x = 3.30$–$3.38\,r_\odot$. We note that the ray was oriented close to the x-axis of LASCO images, i.e., the stacks are roughly perpendicular to the ray direction. The stack-plot contains all images recorded on 8 January 2002 (denoted by an ordinal number on the x-axis of the stack-plot; the time cadence is on average 24 min).

The black/white stripes converging towards the ray location, located at $y \sim 400'' \sim 0.41\,r_\odot$, clearly show inflows into the ray. The corresponding velocities in the left part of the stack-plot are found in the range 15–25 km s^{-1} (mean 19 ± 4 km s^{-1}). These velocities are several times higher than 5 km s^{-1} reported by Yokoyama et al. (2001). After the slice No. 50 (18:54 UT), the stack-plot shows the effects of a large-scale perturbation from another CME, which occurred above the E-limb. We note that the "push" caused by the perturbation increased the inflow speed, which now ranges from 25 to 30 km s^{-1} (mean 27 ± 5 km s^{-1}).

Finally, we note that we also observed intermittent downflows in the form of shrinking loops (similar to that reported by Sheeley et al. 2004), starting from $R \sim 3$. At greater heights, outflows could be discerned, exhibiting at times a pattern similar to that of disconnection events (e.g., Webb & Cliver 1995; Simnett et al. 1997; Wang et al. 1999). This implies that the diffusion region in this event was located around $R \sim 3$, i.e., much higher than in the events shown in Fig. 4.

4. Comparison with the model and previous studies

4.1. Comparison with model predictions

In Fig. 7a, we present a comparison of measurements presented in the fourth column of Fig. 4 with the model-dependencies $\delta n(R)$ that were derived in the Appendix. In particular, we present the model results based on the isothermal ($T = 10^6$ K) Parker (1958) solar-wind model (see also Mann et al. 1999a). For the magnetic field $B(R)$, we consider the empirical coronal magnetic field scaling established by Dulk & McLean (1978). We note that data [a], [b], [d], and [e] have been slightly shifted

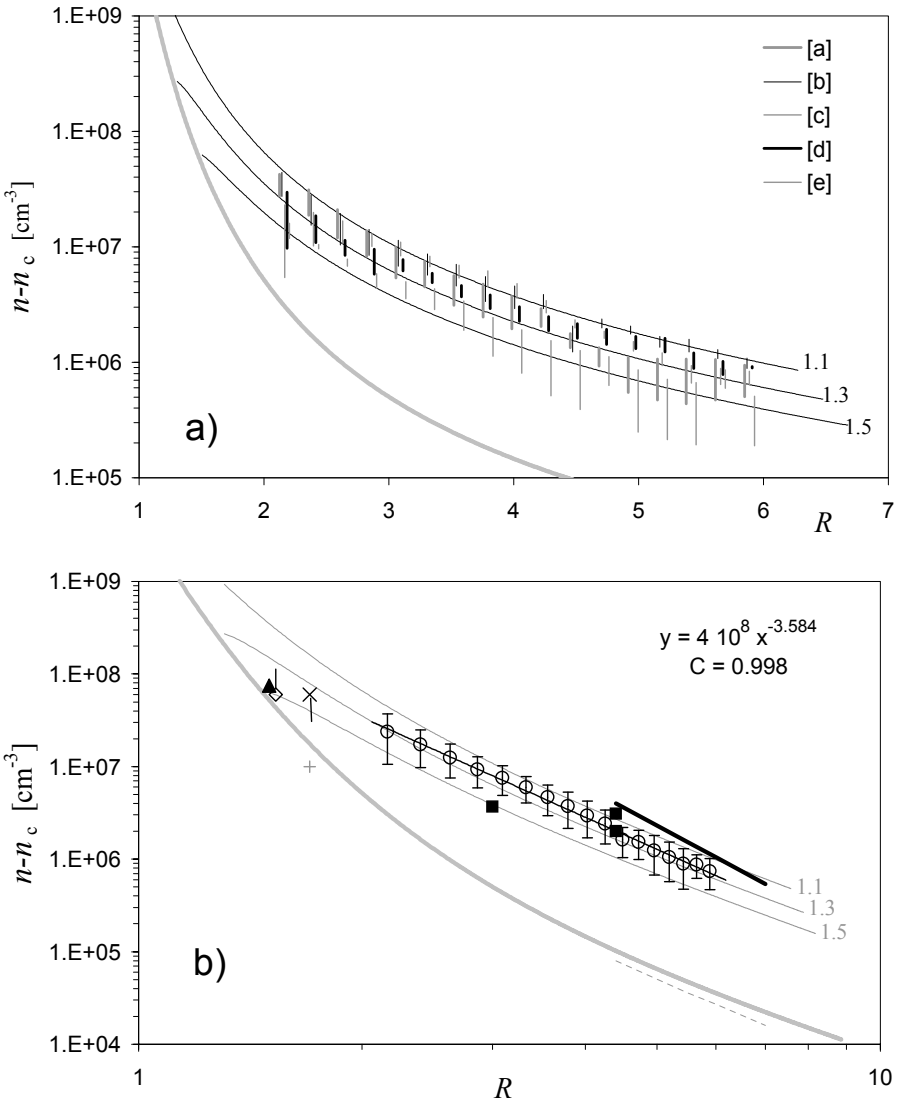

Fig. 7. **a)** Comparison of the density-excess measurements presented in the right hand column of Fig. 4 with the model results (thin black lines labeled by the heliocentric distance of the diffusion region, R_x). Measurements are labeled in the legend, following the sequence in Fig. 4. The thick-gray line shows the density model of a quiet 10^6 K corona (Mann et al. 1999a). **b)** The mean values of the data presented in **a)**, shown by circles with error bars and the corresponding power-law fit (written in the inset), compared with the model results and the values from previous studies reviewed in Sect. 4.2 (diamond – Ko et al. 2003; triangle – Ciaravella et al. 2002; squares – Ko et al. 2003; cross – Bemporad et al. 2006).

along the axis of R-coordinate (symmetrically with respect to [c]) to avoid overlapping. Figure 7a shows clearly that the observations reproduce the model curves well: as stated in Sect. 3.3, the choice of the column length λ_0 only shifts the values up or down, but does not alter the slope. Comparing the trend of the data, we see that the slope corresponds far more closely to the model slopes for the CSs than for the ambient corona. Furthermore, one finds that the CS densities are more than one order of magnitude higher than that in the ambient corona.

In Fig. 7b, we present the measured average density excess $\overline{\delta n}(R)$ (circles with error bars represent the mean values from Fig. 7a with the associated standard deviations) and the corresponding power-law fit, compared with the CS model dependencies. The observational data exhibit the dependence $R^{-3.6}$, whereas for the same height range the CS model data have $\sim R^{-3.0} - R^{-3.2}$ and the quiet-corona model behaves as $R^{-4.3}$ (see Appendix).

4.2. Ray densities from previous studies

Employing various techniques to estimate their density, post-CME rays have been the subject of a number of studies. In Table 1, we present an overview of the spectrographic results obtained from UltraViolet (UV) spectra of five post-CME rays (dates are given in the header row) reported by Ciaravella et al. (2002), Ko et al. (2003), Raymond et al. (2003), Lee et al. (2006), Bemporad et al. (2006), and Ciaravella & Raymond (2008). In the last column, we also present the unpublished results by Schettino et al. (2009, to be submitted).

All rays listed in Table 1 were characterized by the presence of the narrow Fe XVIII emission. UV spectra of rays were obtained with the UltraViolet Coronagraph Spectrometer (UVCS, Kohl et al. 1995) onboard SoHO. The spectrometer observes through a narrow entrance slit 42′ long and up to 84″ wide. The slit can be aligned at any polar angle and at heliocentric distances from 1.5 up to 10 $r_\odot$. UVCS can image spectra of the solar corona in the range 945–1270 Å (473–635 Å in the second order).

The first five rows of Table 1 describe the associated CME/flare events: the first appearance of the CME in the LASCO-C2, the CME mean speed, the soft X-ray importance of the flare if observed, the active region label, and duration of the LASCO-ray if observed, respectively.

The next eight rows concern the ray characteristics as detected in the UV spectra: the time of the first detection of the ray

Table 1. Spectrographic results on the UV current sheets.

	1998 Mar. 23[1]	2002 Jan. 8[2]	2002 Apr. 21[3]	2002 Nov. 26[4]	2003 Nov. 4[5]	2003 June. 2[6]
CME 1st-LASCO	09:33:36	17:54:05	01:27:20	17:06:21	19:54:05	08:54:05
CME speed (km s^{-1})	403	1794	2393	479	2657	980
Flare	N	Ybl*	X 1.5	N	X 30.8	M 3.9
AR No.	—	9782/85	9906	—	10486	10365
LASCO CS	N	2 days	N	N	~20 h	6.5 h
CS obs. start	16:00:30	17:48/Jan 10	00:45:34	18:39:15	20:03:50	09:40:44
CS obs. height	1.51 (– 1.38)	1.53	1.62	1.61	1.69	1.68
CS FWHM width ($r_\odot$)	0.1	0.2	0.3	0.4	0.2–0.1	0.3
CS full width ($r_\odot$)	0.4	0.4	0.6	0.8	0.5–0.2	0.35
CS LoS depth ($r_\odot$)	0.06	0.2	—	0.5	0.1	0.1
CS obs. duration	20 h	10 h	14 min	2.3 days	~17 h	6.3 h
CS temp. (10^6 K)	5	3–4	5	8–3	8–4	7
CS density(10^7 cm^{-3})	5–10	≤4	—	6.5–7.5	7–10	1

[1] Ciaravella et al. (2002); [2] Ko et al. (2003); [3] Raymond et al. (2003); Lee et al. (2006); [4] Bemporad et al. (2006); [5] Ciaravella & Raymond (2008); [6] Schettino et al. (2008, to be submitted). * Ybl = Yes (behind the limb).

by UVCS, the height at which the spectrograph slit intersects the ray, the ray width along the UVCS slit expressed in units of $r_\odot$ (both the full-width at half-maximum and the full width are presented), the estimate of the LoS depth, duration of the ray UVCS observations, and finally, in the last two rows, we present the ray temperature and density.

The ray UVCS densities are presented in Fig. 7b, together with the density-excess measurements presented in Sects. 3.3 and 4.1. The estimate based on the UVCS spectra reported by Ko et al. (2003) is indicated by the diamond symbol. The column-length was assumed therein to be 140 Mm, which was taken to be the same as the FWHM of the spatial profile of the FeXVIII λ974 emission across the post-CME rays. This column-length is about 2 times longer than the value we would obtain for this height by the scaling that was applied in Sect. 3. Thus, to adjust the values to our particular λ_0, the density has to be multiplied by a factor of 2, as indicated by vertical bar attached to the diamond symbol in Fig. 7b.

The density reported by Ciaravella et al. (2002), also estimated from the UVCS data, is indicated by a black triangle. Ciaravella et al. (2002) estimated the CS density at $R = 1.5$ to be $5–10 \times 10^7$ cm^{-3}, assuming a column length of 40 Mm. After adjusting the column-length to its equivalent used in Sect. 3 (a required increase of about 20%), we found the equivalent density of about 6×10^7 cm^{-3}.

The density inferred by Bemporad et al. (2006) from the spectral observations of the face-on current sheet of 26 November 2002 is shown by a black cross. The attached vertical bar indicates that the density could be lower if a larger current sheet thickness were assumed. The gray plus symbol represents the estimated density of the ambient coronal plasma.

In Fig. 7b, we also show (black squares) the density excess data based on the ray and coronal densities estimated by Ko et al. (2003) by employing the LASCO-C2 observations and using the Thompson scattering function (Billings 1966). In estimating the ray density at $R = 4.4$, Ko et al. (2003) assumed a column-length of ~250 Mm, which is about 1.2 times longer than we used at the same height. Thus, adjusting their results to our column-length would reduce the density by a factor of 1.2.

Finally, in Fig. 7b we present the results based on the polarization-brightness measurements performed by Poletto et al. (2008). The thick black line represents the density excess δn re-evaluated from Fig. 9 of Poletto et al. (2008) by applying column-lengths consistent with those applied in Sect. 3. The ray data drawn by the thick line reproduce closely our measurements, whereas the "quiet corona" data (thin gray-dashed line) are close to the model densities.

The power-law fit to all data (adjusted to the same λ_0) shown in Fig. 7b has the slope $R^{-3.3}$ (without the λ_0 adjustment would add up to $R^{-3.0}$). This is quite close to the model slopes found for the radial distance range 1.5–7 $r_\odot$, which are characterized by the power-law exponents 3.0–3.2 for $R_x = 1.1–1.5$ and the Dulk & McLean (1978) magnetic field.

5. Discussion and conclusion

We summarize the empirical characteristics of post-CME rays as follows:

1. Rays often exhibit activity in the form of outflowing features, morphological changes, and changes in inclination, and sometimes we observe reconnection inflows.
2. The width of rays increases with height, from ~0.1–0.3 $r_\odot$ at $R \sim 2$, to ~0.4–0.8 $r_\odot$ at $R \sim 6$.
3. Densities of rays are at least several times (up to more than one order of magnitude) higher than in the ambient corona for the considered height range.
4. The coronal regions surrounding rays are depleted.
5. On average, the number of electrons per unit length of the ray, N_e, first decreases with the height, and then, at greater heights becomes approximately constant.
6. The temperature of rays in the height range $R \sim 1.5–1.7$ ranges from 3 to 8 MK, i.e., it is several times higher than in the "normal" corona, and has a tendency to decrease with time.

The nature of the coronagraphic white-light ray activity is twofold. The formation of fine structure elements, mostly blob-like features, and their outward motion at speeds of 100–1000 km s^{-1}, appears to be the most common internal activity. It could be interpreted in terms of current-sheet tearing, which causes the formation and outward ejection of plasmoids (e.g., Barta et al. 2008; Riley et al. 2007, and references therein). On the other hand, changes in the ray inclination, and morphological changes that could be attributed to changes in the ray geometry,

seem to be caused by the large-scale magnetic-field evolution in the wake of the CME. In some cases, this type of activity is caused by perturbations coming from distant eruptions, most likely large-amplitude waves or shocks.

As stated in item 2, the width increases on average by about $0.4\,r_\odot$ over a distance of $4\,r_\odot$, i.e., the width is roughly proportional to the radial distance. Following our interpretation of rays in terms of the reconnecting current sheet, the ray boundaries should follow the slow-mode shocks. Given the model presented in the Appendix, in particular Fig. A.1, we can conclude that the slow-mode shocks are oriented close to the radial direction, i.e., that the angle denoted in Fig. A.1 as ϕ, is small. Since the angle ϕ (expressed in radians) equals the inflow Alfvén Mach number reduced by the factor n_2/n_1, which represents the density jump at the slow-mode shock (the value of n_2/n_1 depends on β, and should be around 2; see Vršnak & Skender 2005), one finds that the inflow Mach number is low, most likely on the order of 0.01 or less. For higher values, we note that ϕ would be large enough to make the "super-radial" widening of the ray measurable. This may be why inflows such as those shown in Fig. 6 are rarely observed.

We note that the situation shown in Fig. 6 differs from the previously described "stationary" pattern. In this case, we see distinct elongated features inflowing from both sides towards the ray axis of symmetry. Thus, these features cannot be interpreted as CS boundaries, i.e., signatures of the slow-mode shocks, but represent coronal density inhomogeneities aligned with the magnetic field-lines. These features are inclined from the radial direction, i.e., exhibit the "super-radial" orientation. When observed in pairs, they form a V-pattern that is roughly symmetric with respect to the ray axis. Thus, these substructures probably outline the magnetic field inflowing into the current sheet. In this situation, the angle (expressed in radians) between the field-line and the axis of symmetry is equal to the inflow Alfvén Mach number M_A (e.g., Vršnak & Skender 2005). In the event shown in Fig. 6, we estimate this angle to be a few degrees, so we can take $M_A \sim 0.02$–0.05. Since the inflow speed was estimated to be ~ 20 km s^{-1}, this should correspond to the Alfvén speed of 400–1000 km s^{-1}, which seems reasonable for this height range (see, e.g., Vršnak et al. 2004).

The main physical characteristics of post-CME rays are their mass/density excess and increased temperature (Table 1). In addition to the morphology and flows, this can be explained in terms of the reconnection outflow-jet, which is the structural element of the vertical current sheet that forms in the wake of a CME. The measured values of the CS density and the temperature also provide an estimate of the ambient coronal magnetic field, since the external magnetic pressure is roughly equal to the gas pressure in the outflow region (see, e.g., Appendix in Aurass et al. 2002). Using the values $n_{CS} = 5$–10×10^7 cm^{-3} and $T_{CS} = 5$–8 MK, we find that the ambient magnetic field is $B_c \sim 0.9$–1.7 Gauss. Such a value is consistent with the empirical scaling $B = 0.5(R-1)^{-1.5}$ established by Dulk & McLean (1978), which infers that $B \sim 0.85$–1.41 Gauss for the radial distance range $R = 1.5$–1.7. Similarly, by using the relationship between the temperature jump at SMSs and the external plasma-to-magnetic pressure ratio, $T_2/T_1 = 1 + 0.4/\beta$ (see Eq. (12) in Aurass et al. 2002), we can find the value of β in the inflow region. Applying $T_2/T_1 \lesssim T_{CS}/T_c = 2$–$8$, we find $\beta \gtrsim 0.4$–0.06. These values are approximately consistent with those expected for the active region corona in this height range (Gary 2001).

Based on the quasi-stationary Petschek (1964) reconnection regime, the results of the model are consistent with the observed density excesses. At the standing slow-mode shocks, formed by the CS inflow, the plasma is heated, compressed, and accelerated/deflected to form the upward directed reconnection jet. In this way, the dense plasma from the low corona is transported to greater heights, causing the observed density excess. Model results show that the density can increase by more than an order of magnitude, which is consistent with observations. However, we note that the observed values depend on the assumed value of the LoS CS-depth λ_0. Our results indicate that λ_0 is on the order of 100 Mm, and that the plane of the observed rays is inclined at small angles with respect to the LoS.

The parameter that does not depend on the LoS CS-depth, or the CS orientation, is the number of electrons per unit length of the CS, which we denoted in Sect. 3.3 as N_e. The measurements indicate that $N_e(R)$ either decreases, or is approximately constant. On average, $N_e(R)$ first decreases and then becomes approximately constant at $R_c \sim 4$. Given our observations, as well as the observations by Ciaravella & Raymond (2008), it seems that R_c differs between different events.

Bearing in mind the equation of continuity, there are two effects that determine the radial dependence of N_e. One is the radial dependence of the reconnection-outflow velocity, and the other is the contribution of the inflowing plasma. For example, if the outflow speed is constant, the value of N_e should increase monotonously with height due to the cumulative supply of the plasma through the SMSs (as more and more inflowing plasma joins the outflow). On the other hand, if the inflow contribution is negligible (as it is at great heights), then a decelerated outflow should be associated with increasing $N_e(R)$, whereas an accelerated outflow should relate to a decreasing $N_e(R)$.

Inspecting outcomes for various model inputs, we found that regardless of the model details, in the vicinity of the diffusion region $N_e(R)$ increases steeply due to the strong effect of the plasma inflow. At greater heights, higher than $\sim 0.5\,r_\odot$ above the diffusion region, the behavior of $N_e(R)$ becomes dependent on the model input. An agreement with observations (decreasing $N_e(R)$ followed by $N_e \sim$ const.) is found only for cases where the Alfvén velocity and the solar-wind speed increase within the given height range, and only if the diffusion region is below $R \sim 1.4$. Given that the power-law fit presented in Fig. 5b describes quite accurately the $N_e(R)$ dependence in the form $N_e \propto R^{-1}$, the outflow velocity should increase approximately as $v_{out} \propto R$. However, we note that the last three data-points in Fig. 5b might indicate that N_e starts to increase gradually beyond $R \sim 5$. This behavior is found in all of the considered model options, i.e., after the solar-wind speed becomes approximately constant and the Alfvén velocity begins to decrease, the value of N_e gradually increases with radial distance.

In this respect, we emphasize that the model results generally depend on the applied coronal density and magnetic-field model. On the other hand, the $N_e(R)$ measurements are affected by large errors in estimating the ray width D. Since the comparison between observed and calculated $N_e(R)$ might lead to ambiguous conclusions, we find that the most reliable model-parameter to compare with observations is the slope of the $n_{CS}(R)$ dependence, which should be less steep than the slope of the ambient $n_c(R)$, regardless of the model details. Comparing the calculated and observed slopes, we find good correspondence.

Finally, the model predicts a decrease in the density excess with time, due to a rise in the diffusion region height. Since this rise is slow, we expect the decrease in the density excess to be similarly slow. Indeed, we did not detect any decrease in the ray density within 12 h interval analyzed in the ray of 9 January 2002. However, we note that a decrease of the density was reported by Ciaravella & Raymond (2008) in the event of

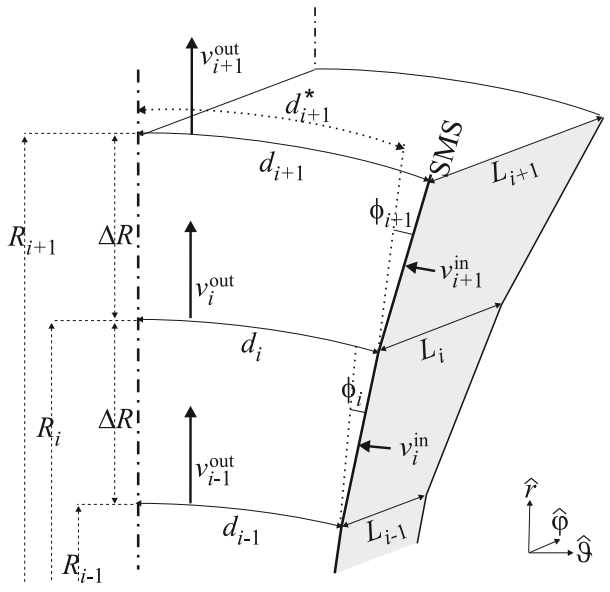

Fig. A.1. Geometry of the post-CME ray model. Dash-dotted lines depict the axis of symmetry, shaded area represents the slow mode shock (SMS) and dotted lines the local radial direction. Local coordinate system is indicated in the lower-right corner. For details see the text in the Appendix.

4 November 2003. From their Table 1 we find that the density decreased by ~40–50% in about 2 h. According to our model, such a decrease would correspond to an increase of the diffusion region height for $\Delta R \sim 0.1$, which would correspond to the rise speed on the order of 10 km s^{-1}. On the other hand, given the accuracy of our density estimates (~50%), we infer that in the event of 9 January 2002 the rise speed of the diffusion region was less than 2 km s^{-1}.

Acknowledgements. We thank ISSI (International Space Science Institute, Bern) for the hospitality provided to the members of the team on the Role of Current Sheets in Solar Eruptive Events where many of the ideas presented in this work have been discussed. G.P. acknowledges support from ASI/INAF I/015/07/0.

Appendix A

The overall geometry of the post-CME ray, which is assumed to be a signature of the bifurcated, reconnecting current-sheet, is shown in Fig. A.1. The diffusion region, where the magnetic field lines reconnect, is located at the radial distance R_x. The oppositely directed field lines merge at the velocity $v_{in}(R)$, bringing the coronal plasma of density $\rho_c(R)$ into the reconnection outflow jet (the ray). We assume that the merging velocity is higher than the local slow-mode speed, so the slow-mode shocks (SMSs) form in between the two inflows, bounding the reconnection outflow as in the Petschek (1964) reconnection model.

Given the spherical geometry of the corona, the flow velocity vector in the inflow region can be represented as a superposition of the radial component (corresponding to the solar wind speed v_{sw}) and the "horizontal" component v_{in} (the direction of the unit vector $\hat{\vartheta}$ being shown in the lower-right corner of Fig. A.1), as depicted in Fig. 1b.

In the stationary state, the relation $\nabla \times \boldsymbol{E} = 0$ must be satisfied, to provide $\partial \boldsymbol{B}/\partial t = 0$. In a spherical coordinate system (see the lower-right corner of Fig. A.1), this implies that $\partial(rE_{\hat{\varphi}})/\partial r = 0$, i.e., $Rv_{in}B = \text{const}$. To describe the ambient coronal magnetic field $B(R)$, we consider the empirical model of Dulk & McLean (1978) and the simple analytical model of Mann et al. (1999b; see also Vršnak et al. 2002), which then defines $v_{in}(R)$.

We denote the angle between the radial direction and the slow-mode shock (Fig. A.1) as $\phi(R)$. Taking into account the continuity equation across the SMS

$$v_{in}\rho_c \Delta R = v_{out}\rho_{SMS}\Delta R\,\phi\,, \tag{A.1}$$

where $v_{out} \sim v_A + v_{sw}$ (Skender et al. 2003; Vršnak & Skender 2005), we find

$$\phi = \frac{\rho_c}{\rho_{SMS}}\,\frac{v_{in}}{v_A + v_{sw}}, \tag{A.2}$$

which defines the geometry of the SMSs.

To describe the coronal mass density $\rho_c(R)$, we use the isothermal solar-wind model of Parker (see Mann et al. 1999a) for temperature $T_c = 1$, 1.5, and 2 MK, which also provides the corresponding solar-wind speed $v_{sw}(R)$. This, together with the previously defined $B(R)$, also defines the ambient coronal Alfvén velocity $v_A(R)$ and plasma-to-magnetic pressure ratio $\beta(R)$, which both govern the jump relations at the SMS. Assuming that the guiding field is negligible, the density and temperature jump at SMS can be expressed as:

$$\frac{\rho_{SMS}}{\rho_c} = \frac{5(1+\beta)}{2+5\beta}, \tag{A.3}$$

$$\frac{T_{SMS}}{T_c} = 1 + \frac{2}{5\beta}, \tag{A.4}$$

(Aurass et al. 2002; Skender et al. 2003; Vršnak & Skender 2005), which determines the density and the temperature of the plasma inflowing into the reconnection outflow jet at a given R.

At a given radial distance R, the density of the reconnection outflow is determined by both the flow carried from lower heights and the flow carried across the SMS. According to the geometry depicted in Fig. A.1, the continuity equation (mass conservation) can be written in the form:

$$\rho_{i+1}^{out} v_{i+1}^{out} L_{i+1} d_{i+1} = \rho_i^{out} v_i^{out} L_i d_i + \rho_{i+1}^{in} v_{i+1}^{in} \overline{L}_{i+1} \Delta R, \tag{A.5}$$

where $\overline{L}_{i+1} \equiv (L_i + L_{i+1})/2$, $\rho_{i+1}^{in} \equiv \rho^{in}(\overline{R}_{i+1})$, and $v_{i+1}^{in} \equiv v^{in}(\overline{R}_{i+1})$ are the current sheet length, the ambient density, and the ambient velocity at $R = \overline{R}_{i+1} \equiv R_i + \Delta R/2$, respectively. The term on the left-hand side represents the mass flow through the upper surface $L_{i+1} \times d_{i+1}$, where L represents the length of the current sheet perpendicular to the plane of Fig. A.1. The first term on the right-hand side represents the mass flow through the bottom surface $L_i \times d_i$ and the second one the inflow across the SMS. The flow speeds v^{out} can be estimated as $v_i^{out} = v_A(R_i) + v_{sw}(R_i)$ and $v_{i+1}^{out} = v_A(R_{i+1}) + v_{sw}(R_{i+1})$.

Assuming the spherical geometry, the length L is given by

$$L(R) = L(R_x)\frac{R}{R_x}, \tag{A.6}$$

where R_x is the radial distance of the diffusion region and $L(R_x)$ is the current sheet extension in the $\hat{\varphi}$-direction at R_x, i.e., it represents the length of the current sheet X-line. The width of the current sheet at a given radial distance can be evaluated using

$$d_{i+1} = d_i\,\frac{R_{i+1}}{R_i} + \Delta R\,\phi_{i+1}, \tag{A.7}$$

with $d_x \equiv d(R_x) \sim 0$, i.e., $d_1 = \phi_1 \Delta R$. The first term on the right-hand side of Eq. (A.7) is determined by the spherical geometry

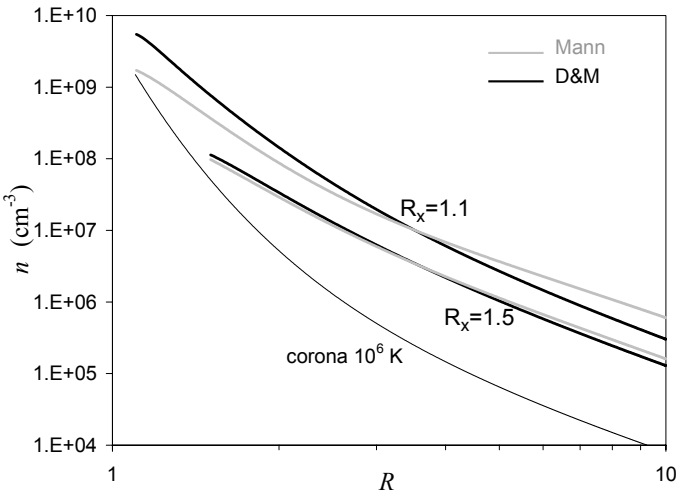

Fig. A.2. Current sheet number-density calculated using the coronal magnetic field model by Dulk & McLean (1978) and Mann et al. (1999b); thick-black and thick-gray lines, respectively. The solar wind density model by Mann et al. (1999a) is drawn by thin-gray line (denoted as "corona 10^6 K").

(hereinafter we abbreviate $d_i R_{i+1}/R_i \equiv d^*_{i+1}$, i.e., $d_{i+1} = d^*_{i+1} + \Delta R\,\phi_{i+1}$), and the second term is related to the inclination of the SMS with respect to the local radial direction (Fig. A.1).

Equations (A.1–A.7) estimate the density distribution along the post CME-ray, $\rho_{\rm out}(R)$, for various values of diffusion region height $R_{\rm x}$. In Fig. A.2, we show the results obtained using the coronal magnetic-field model of Dulk & McLean (1978) and Mann et al. (1999b), whereas for the coronal density, we use the isothermal (10^6 K) solar-wind model of Mann et al. (1999a).

We now consider the plasma temperature along the current sheet. In the first layer above the X-line, the temperature equals the temperature $T_{\rm SMS}$ evaluated by Eq. (A.4) at the radial distance $R = \overline{R}_1 \equiv R_{\rm x} + \Delta R/2$. The plasma of this temperature moves outward and enters into the next layer through the area $d_1 \times L_1$, undergoing adiabatic cooling due to volume expansion. In the second layer, it meets with the plasma that enters into the current sheet through the slow-mode shock, where it is heated to $T_{\rm SMS}(\overline{R}_2)$. The same happens successively in each additional level.

Since the thermal conductivity of coronal plasma is very high, the temperature can be assumed to be uniform across each layer, i.e., along the magnetic field-lines connecting the SMSs (i.e., magnetic-field component B_ϑ). Thus, we can write for the temperature of a given layer:

$$T_{\rm CS} = \frac{m_d T_d + m_{\rm SMS} T_{\rm SMS}}{m_d + m_{\rm SMS}}, \tag{A.8}$$

where, m_d and T_d are the mass and temperature, respectively, of the plasma contained in the volume defined by the lines denoted in Fig. A.1 as d_i and d^*_{i+1}. We note that we have neglected the thermal conductivity along the CS axis of symmetry, since the heat flow in this direction is reduced due to the magnetic-field component B_ϑ, and the temperature gradients are small due to the large vertical length-scale of the CS. The mass m_d is determined by:

$$m_d^{i+1} = \frac{\rho_{i+1} + \rho_i}{2} \Delta R\, \frac{L_{i+1} + L_i}{2}\, \frac{d^*_{i+1} + d_i}{2}, \tag{A.9}$$

whereas $m_{\rm SMS}$ and $T_{\rm SMS}$ are the mass and temperature of the plasma contained in the "triangular" volume between the radial and the slow mode shock. The temperature $T_{\rm SMS}$ can be evaluated by Eq. (A.4) at the radial distance $R = \overline{R}_{i+1} \equiv R_i + \Delta R/2$, and the mass $m_{\rm SMS}$ is determined by:

$$m^{i+1}_{\rm SMS} = \rho^{i+1}_{\rm SMS} \Delta R\, \frac{L_{i+1} + L_i}{2}\, \frac{\Delta R \phi_{i+1}}{2}\,. \tag{A.10}$$

where $\rho^{i+1}_{\rm SMS}$ is evaluated by Eq. (A.3) at the radial distance $R = \overline{R}_{i+1} = R_i + \Delta R/2$.

The estimate of the temperature $T_{\rm CS}$ in a given layer still requires evaluation of the temperature T_d, where we must take account of the adiabatic expansion from the layer "i" to "$i+1$". The plasma contained in the volume defined by lines d_{i-1} and d_i:

$$V_i = \Delta R\, \frac{L_i + L_{i-1}}{2}\, \frac{d_i + d_{i-1}}{2}, \tag{A.11}$$

expands into the volume:

$$V_{i+1} = \Delta R\, \frac{L_{i+1} + L_i}{2}\, \frac{d^*_{i+1} + d_i}{2} + (L_{i+1} d^*_{i+1} v^{\rm out}_{i+1} - L_i d_i v^{\rm out}_i)\Delta t. \tag{A.12}$$

The time Δt can be expressed as

$$\Delta t = \frac{\Delta R}{\overline{v}^{\rm out}_{i+1}}, \tag{A.13}$$

where $\overline{v}^{\rm out}_{i+1} = (v^{\rm out}_{i+1} + v^{\rm out}_i)/2$. The difference between the first term on the right-hand-side of Eq. (A.12) and v_i is related to the expansion in $\hat{\varphi}$ and $\hat{\vartheta}$ directions, whereas the second term on the right-hand-side of Eq. (A.12) represents the contribution of the expansion in the $\hat{r}$-direction. Bearing in mind the characteristics of the adiabatic expansion, we obtain:

$$T^{i+1}_d = T^i_{\rm CS} \left(\frac{V_i}{V_{i+1}}\right)^{(\gamma-1)}, \tag{A.14}$$

where γ is the ratio of the specific heats, which for hydrogen plasma equals to $\gamma = 5/3$.

The system of Eqs. (A.1–A.14) can be solved starting from the first layer above the diffusion region, and successively calculating the values in every new layer by using the values obtained for previous layer. In this way, we derive the dependencies $\rho(R)$ and $T(R)$ for the current sheet plasma.

References

Asai, A., Yokoyama, T., Shimojo, M., & Shibata, K. 2004, ApJ, 605, L77
Aschwanden, M. J., Kosugi, T., Hudson, H. S., Wills, M. J., & Schwartz, R. A. 1996, ApJ, 470, 1198
Aurass, H., Vršnak, B., & Mann, G. 2002, A&A, 384, 273
Bárta, M., Vršnak, B., & Karlický, M. 2008, A&A, 477, 649
Bemporad, A., Poletto, G., Suess, S. T., et al. 2006, ApJ, 638, 1110
Bemporad, A., Poletto, G., Landini, F., & Romoli, M. 2008, Ann. Geophys., in press
Billings, D. E. 1966, A guide to the solar corona (New York: Academic Press)
Brueckner, G. E., Howard, R. A., Koomen, M. J., et al. 1995, Sol. Phys., 162, 357
Carmichael, H. 1964, in The Physics of Solar Flares, ed. W. N. Hess, 451
Ciaravella, A., & Raymond, J. C. 2008, ApJ, in press
Ciaravella, A., Raymond, J. C., Li, J., et al. 2002, ApJ, 575, 1116
Dulk, G. A., & McLean, D. J. 1978, Sol. Phys., 57, 279
Forbes, T. G., & Acton, L. W. 1996, ApJ, 459, 330
Forbes, T. G., Linker, J. A., Chen, J., et al. 2006, Space Sci. Rev., 123, 251
Furth, H. P., Killeen, J., & Rosenbluth, M. N. 1963, Physics of Fluids, 6, 459
Gary, G. A. 2001, Sol. Phys., 203, 71
Gekelman, W., & Pfister, H. 1988, Physics of Fluids, 31, 2017
Hirayama, T. 1974, Sol. Phys., 34, 323
Innes, D. E., McKenzie, D. E., & Wang, T. 2003a, Sol. Phys., 217, 247
Innes, D. E., McKenzie, D. E., & Wang, T. 2003b, Sol. Phys., 217, 267
Ko, Y.-K., Raymond, J. C., Lin, J., et al. 2003, ApJ, 594, 1068

Kohl, J. L., Esser, R., Gardner, L. D., et al. 1995, Sol. Phys., 162, 313
Kopp, R. A., & Pneuman, G. W. 1976, Sol. Phys., 50, 85
Lee, J.-Y., Raymond, J. C., Ko, Y.-K., & Kim, K.-S. 2006, ApJ, 651, 566
Lin, J. 2004, Sol. Phys., 219, 169
Lin, J., Ko, Y.-K., Sui, L., et al. 2005, ApJ, 622, 1251
Mann, G., Jansen, F., MacDowall, R. J., Kaiser, M. L., & Stone, R. G. 1999a, A&A, 348, 614
Mann, G., Klassen, A., Estel, C., & Thompson, B. J. 1999b, in 8th SOHO Workshop: Plasma Dynamics and Diagnostics in the Solar Transition Region and Corona, ed. J.-C. Vial, & B. Kaldeich-Schü, ESA SP, 446, 477
Maričić, D., Vršnak, B., Stanger, A. L., et al. 2007, Sol. Phys., 241, 99
Masuda, S., Kosugi, T., Hara, H., Tsuneta, S., & Ogawara, Y. 1994, Nature, 371, 495
McKenzie, D. E., & Hudson, H. S. 1999, ApJ, 519, L93
Parker, E. N. 1958, ApJ, 128, 664
Petschek, H. E. 1964, in The Physics of Solar Flares, ed. W. N. Hess, 425
Poland, A. I., Howard, R. A., Koomen, M. J., Michels, D. J., & Sheeley, Jr., N. R. 1981, Sol. Phys., 69, 169
Poletto, G., Bemporad, A., Landini, F., & Romoli, M. 2008, Ann. Geophys., in press
Raymond, J. C., Ciaravella, A., Dobrzycka, D., et al. 2003, ApJ, 597, 1106
Riley, P., Linker, J. A., Mikić, Z., et al. 2002, ApJ, 578, 972
Riley, P., Lionello, R., Mikić, Z., et al. 2007, ApJ, 655, 591
Roussev, I. I., Forbes, T. G., Gombosi, T. I., et al. 2003, ApJ, 588, L45
Saez, F., Llebaria, A., Lamy, P., & Vibert, D. 2007, A&A, 473, 265
Sheeley, Jr., N. R., & Wang, Y.-M. 2002, ApJ, 579, 874
Sheeley, Jr., N. R., & Wang, Y.-M. 2007, ApJ, 655, 1142
Sheeley, Jr., N. R., Warren, H. P., & Wang, Y.-M. 2004, ApJ, 616, 1224
Simnett, G. M., Tappin, S. J., Plunkett, S. P., et al. 1997, Sol. Phys., 175, 685
Skender, M., Vršnak, B., & Martinis, M. 2003, Phys. Rev. E, 68, 046405
Soward, A. M., & Priest, E. R. 1982, J. Plasma Physics, 28, 335
Sturrock, P. A. 1966, Nature, 211, 695
Sui, L., Holman, G. D., & Dennis, B. R. 2004, ApJ, 612, 546
Sui, L., Holman, G. D., White, S. M., & Zhang, J. 2005, ApJ, 633, 1175
Švestka, Z. F., Fontenla, J. M., Machado, M. E., Martin, S. F., & Neidig, D. F. 1987, Sol. Phys., 108, 237
Török, T., Kliem, B., & Titov, V. S. 2004, A&A, 413, L27
Tsuneta, S. 1996, ApJ, 456, 840
Tsuneta, S., Hara, H., Shimizu, T., et al. 1992, PASJ, 44, L63
Ugai, M. 1987, Geophys. Res. Lett., 14, 103
Veronig, A. M., Karlický, M., Vršnak, B., et al. 2006, A&A, 446, 675
Vourlidas, A., Buzasi, D., Howard, R. A., & Esfandiari, E. 2002, in Solar Variability: From Core to Outer Frontiers, ed. J. Kuijpers, ESA SP, 506, 91
Vourlidas, A., Subramanian, P., Dere, K. P., & Howard, R. A. 2000, ApJ, 534, 456
Vršnak, B. 2008, Annales Geophysicae, 26, 3089
Vršnak, B., & Skender, M. 2005, Sol. Phys., 226, 97
Vršnak, B., Magdalenić, J., Aurass, H., & Mann, G. 2002, A&A, 396, 673
Vršnak, B., Klein, K.-L., Warmuth, A., Otruba, W., & Skender, M. 2003, Sol. Phys., 214, 325
Vršnak, B., Magdalenić, J., & Zlobec, P. 2004, A&A, 413, 753
Vršnak, B., Temmer, M., Veronig, A., Karlický, M., & Lin, J. 2006, Sol. Phys., 234, 273
Wang, Y.-M., Sheeley, N. R., Howard, R. A., St. Cyr, O. C., & Simnett, G. M. 1999, Geophys. Res. Lett., 26, 1203
Webb, D. F., & Cliver, E. W. 1995, J. Geophys. Res., 100, 5853
Webb, D. F., Burkepile, J., Forbes, T. G., & Riley, P. 2003, J. Geophys. Res. (Space Physics), 108, 1440
Yokoyama, T., Akita, K., Morimoto, T., Inoue, K., & Newmark, J. 2001, ApJ, 546, L69